Small Structures

small structures

www.small-structures.com

RESEARCH ARTICLE OPEN ACCESS

Structural Inheritance Synthesis of Multidimensional Germanium Nanostructures and Their Structure-Performance Correlations in Lithium Storage

Ben Pu[1] | Yue Qing[1] | Yan Liu[1] | Yongbin Wang[1] | Ceping Yu[1] | Luning Zhang[1] | Rongman Sun[1] | Bin Zhou[2] | Weiqing Yang[1,3]

[1]Key Laboratory of Advanced Technologies of Materials (Ministry of Education), School of Materials Science and Engineering, Southwest Jiaotong University, Chengdu, P R China | [2]Sichuan Research Center of New Materials, Institute of Chemical Materials, China Academy of Engineering Physics, Chengdu, P R China | [3]Research Institute of Frontier Science, Southwest Jiaotong University, Chengdu, P R China

Correspondence: Yan Liu (y_liu@swjtu.edu.cn) | Bin Zhou (bzhou@caep.cn) | Weiqing Yang (wqyang@swjtu.edu.cn)

Received: 20 October 2025 | **Revised:** 27 November 2025 | **Accepted:** 11 December 2025

Keywords: anode materials | galvanic replacement | germanium nanomaterials | lithium-ion batteries | structural inheritance

ABSTRACT

The unique properties and structural merits of multidimensional germanium (Ge) nanostructures have enabled their broad applications in energy storage, biomedical engineering, and sensor technologies. Nevertheless, the current synthesis strategies for Ge nanostructures are highly reliant on size-specific control methods, while achieving controllable fabrication of multidimensional nanostructures under a unified scale range constraint remains a critical challenge. Herein, we present a precisely controlled galvanic replacement reaction strategy for the structural inheritance synthesis of multidimensional Ge nanostructures, establishing clear structure-performance relationships for enhanced lithium storage. A remarkable rate capability is achieved in engineered Ge nanostructures, showing specific capacities of 24.2, 15.2, and 9.0 times that of bulk Ge at 10 A g^{-1} for NWs, NPs, and NSs, respectively. Particularly, the NWs exhibited superior cycling stability, maintaining a reversible capacity as high as 1,132 mAh g^{-1} after 200 cycles at 1 A g^{-1}. The exceptional electrochemical enhancement originates from effective interfacial stress mitigation during lithium alloying/dealloying processes and optimized charge–transfer kinetics enabled by nanostructural engineering, as systematically verified through electrochemical kinetic analyses. This work proposes a universal synthesis method for multidimensional alloy-type anode materials, reveals the structure-performance correlations, and offers valuable insights for the design of high-performance energy storage materials.

1 | Introduction

Germanium (Ge) nanostructures have emerged as versatile functional materials due to their quantum confinement effects and tunable surface chemistry, enabling tailored applications across energy storage, biomedical engineering, infrared optoelectronics, and catalytic conversion technologies [1–7]. Zero-dimensional Ge nanoparticles (NPs), for example, demonstrate significant potential in antimicrobial nanotherapeutics [8], photothermal therapy [9], and third-generation photovoltaic devices [10]. One-dimensional Ge nanowires (NWs) offer distinct advantages in high-sensitivity piezoresistive sensors [11], high-rate alkali-ion battery anodes [12–14], and broadband photodetectors [15, 16]. Two-dimensional Ge nanosheets (NSs) exhibit exceptional properties for mid-infrared plasmonics [7, 17, 18], biodegradation [19], and interfacial charge storage [20], which are attributed to their anisotropic electron transport properties.

Ben Pu and Yue Qing contributed equally to this work.

This is an open access article under the terms of the Creative Commons Attribution License, which permits use, distribution and reproduction in any medium, provided the original work is properly cited.

© 2025 The Author(s). *Small Structures* published by Wiley-VCH GmbH.

To fabricate Ge nanostructures with tailored architectures, researchers have developed a variety of synthesis methods. For example, Yang et al. [21] prepared three-dimensional nanoporous Ge via a dealloying approach, which involves melting and casting metal ingots followed by acid etching to remove excess metal. Despite its simplicity, this method requires high temperatures (>700°C) and is generally restricted to producing 3D porous morphologies. Metallothermic reduction [22, 23] and gas-phase reduction [24–27] methods utilize reducing agents (e.g., metallic zinc or H_2) to reduce GeO_2 into metallic Ge. These processes still depend on high temperatures (>400°C) and involve additional steps such as acid washing to remove byproducts or require sealed environments for safe hydrogen handling. Moreover, they typically yield only porous nanomaterials due to the removal of oxygen atoms from the GeO_2 framework. Chemical vapor deposition (CVD) is another widely adopted technique for producing Ge nanostructures like NWs [28, 29] and nanotubes [30]. Nonetheless, CVD also operates at elevated temperatures (>400°C), often under vacuum and employs hazardous precursors such as germane (GeH_4), introducing considerable operational risks. Li et al. [31] employed electrospinning, which reduces the reaction temperature (<300°C) and can be conducted in air, yet this method suffers from low production efficiency, process instability, and high-voltage hazards and is limited to generating NWs. Electrochemical deposition [32–34] represents another route offering high efficiency and good controllability. However, it usually requires templates, and the nanostructures are often damaged during template removal. Issues such as poor reproducibility, nonuniform deposition, and uncontrollable morphology pose significant challenges to its utility. Additionally, the energy consumption associated with the required electric field is another factor that must be considered. In comparison, wet chemical synthesis [35, 36] holds considerable promise for its mild reaction conditions, rapid processing, and avoidance of high temperature or vacuum. However, this solution-based crystallization method not only often leads to poorly controlled morphology but also frequently requires the use of the highly toxic solvent trioctylphosphine (TOP) [2, 37]. Furthermore, the relatively low reduction potential of Ge^{2+} makes the solution-phase synthesis of defined Ge nanostructures particularly difficult. In summary, most existing methods suffer from energy-intensive high-temperature requirements, complex equipment, or a lack of versatility.

To overcome these challenges, we developed a dimensionally programmable strategy based on a galvanic replacement reaction (GRR), enabling the rapid (within 8 h) and high-yield synthesis of well-defined Ge nanostructures—including zero-dimensional particles (0D NPs), one-dimensional nanowires (1D NWs), and two-dimensional nanosheets (2D NSs)—through structural inheritance from redox-active Cu nano-templates. Importantly, the process operates at a relatively low temperature (240°C) and utilizes the environmentally benign solvent DMPU as a safer and more sustainable alternative to TOP, thereby significantly improving the sustainability and safety. Leveraging mild reaction conditions and readily available precursors, this approach offers an efficient, scalable synthetic route that effectively addresses key limitations of existing techniques. The as-synthesized Ge nanostructures were systematically evaluated as advanced anode materials in lithium-ion batteries (LIBs), revealing intrinsic correlations between dimensionality and electrochemical storage behavior. Electrochemical evaluations revealed exceptional rate performance with specific capacities of 516.9 mAh g^{-1} (NWs), 326.1 mAh g^{-1} (NPs), and 193.5 mAh g^{-1} (NSs) at 10 A g^{-1}, corresponding to enhancements of 24.2, 15.2, and 9.0 times over bulk Ge (21.4 mAh g^{-1}). The Ge nanostructures (NWs, NPs, and NSs) exhibited outstanding stability after 200 cycles at 1 A g^{-1}, achieving 4.6-, 3.0-, and 3.6-fold higher reversible capacities than bulk Ge, respectively. The enhanced performance stems from synergistic effects including high ionic accessibility, mitigated volume variations, and improved electron transport, collectively alleviating pulverization issues common in alloy-type electrodes. A comprehensive electrochemical kinetic investigation, employing electrochemical impedance spectroscopy (EIS), cyclic voltammetry (CV), and galvanostatic intermittent titration technique (GITT), unveils synergistic enhancement mechanisms: (i) nanoconfinement-induced interfacial stress relaxation, and (ii) hierarchical structure-driven charge–transfer acceleration. Significantly, the 1D NW configuration forms 3D percolation networks that simultaneously provide continuous electron pathways and mechanical buffering spaces. This GRR-based synthetic strategy presents universal applicability in fabricating diverse alloy-type nanostructures (Sb, Bi, Sn) featuring programmable architectures, and provides insights into the material design of next-generation energy storage systems.

2 | Results and Discussion

2.1 | Synthesis and Characterization of Multidimensional Ge Nanomaterials

Figure 1 illustrates our dimensionally programmable synthesis strategy, where structural inheritance from sacrificial Cu templates enables precise morphological control. The three-stage process involves the following: (i) template engineering of 0D Cu NPs (via thermal decomposition), 1D Cu NWs (via hydrothermal growth), and 2D Cu NSs (via roller pressing techniques) (Figures S1 and S2); (ii) an interface-dominated galvanic replacement reaction (GRR) driven by redox potential modulation; and (iii) phase-pure Ge nanostructure formation via ion exchange. The Cu templates play dual roles: as structural scaffolds enabling dimensional control via epitaxial confinement, and as electron donors for Ge^{2+} reduction. The thermodynamic barrier is overcome via iodide-mediated potential alignment ($E^{\theta}(Cu^{+}/Cu)$ =

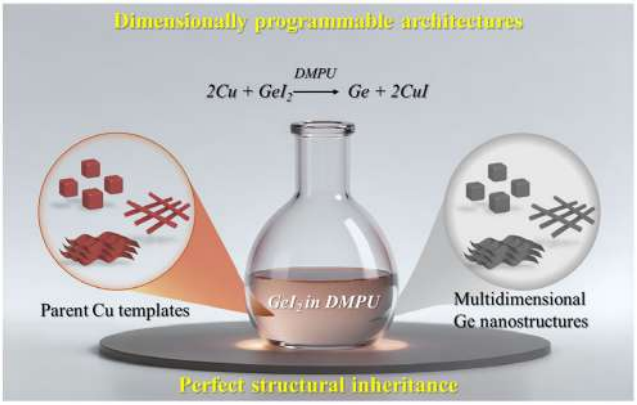


FIGURE 1 | Schematic illustration of the synthesis routes for the 0D Ge NPs, 1D Ge NWs, and 2D Ge NSs.

26884062, 2026, 1, Downloaded from https://onlinelibrary.wiley.com/doi/10.1002/sstr.202500755, Wiley Online Library on [06/11/2026]. See the Terms and Conditions (https://onlinelibrary.wiley.com/terms-and-conditions) on Wiley Online Library for rules of use; OA articles are governed by the applicable Creative Commons License

+0.521 V > $E^{\theta}(Ge^{2+}/Ge)$ = +0.1 V) (Table S1), with the interfacial potential gradient (Note S1, ΔE = +0.1397 V) calculated using the Nernst equation. This design principle enables the spontaneous reaction: $2Cu + GeI_2 \rightarrow Ge + 2CuI$. Trioctylphosphine (TOP) was chosen as the optimal solvent owing to its exceptional GeI_2 solubility, strong CuI complexation, and catalytic role in activating the Ge—I bond cleavage [2]. Guided by green chemistry principles, we engineered a solvothermal synthesis in less-toxic DMPU (N,N'-dimethylpropyleneurea) [38] through kinetic modulation of precursor concentration (1:0.6–1:1.2), temperature (200°C–240°C), and reaction time (4–8 h). This approach achieved high-purity Ge NWs (Figures S3 and S4) while eliminating traditional high-toxic solvents (TOP).

The synthesized multidimensional Ge nanostructures were characterized in terms of their structure and crystalline phase, with the results presented in Figure 2. The X-ray diffraction (XRD) patterns in Figure 2a show that all Ge nanostructures exhibit the characteristic diamond cubic structure (JCPDS No. 04-0545) [39], confirming the successful synthesis of pure-phase Ge nanostructures via transformation from Cu templates. The structural information of the Ge nanomaterials was further verified through Raman spectroscopy. As shown in Figure 2b, the characteristic E_{2g} phonon mode [7, 40–42] of diamond-cubic Ge exhibits a sharp resonance at 290 cm^{-1}. The agreement between the XRD and Raman spectroscopy results substantiates the stability and reproducibility of the proposed methodology under identical conditions. XPS depth profiling elucidates the surface chemistry evolution during galvanic replacement. The survey spectrum [43] (Figure 2c) confirms complete Cu removal, as no signals related to Cu were observed. High-resolution Ge 3d analysis (Figure 2d) deconvolutes two chemical states: metallic Ge–Ge (29.0 eV) and surface GeO_x (32.2 eV) [43, 44]. But no signal of GeO_x was detected in either XRD or Raman analyses, indicating that oxidation is confined to the material surface.

The structural evolution from Cu templates to Ge nanostructures was systematically investigated through scanning electron microscopy (SEM) and transmission electron microscopy (TEM). As shown in Figures 3a1–c2 and S5, the synthesized 0D Ge NPs (70 nm), 1D Ge NWs (diameter: 70 nm), and 2D Ge NSs (thickness: 80 nm) exhibit high dimensional inheritance from their parent Cu templates (Figure S2), validating the precision of the galvanic replacement for programmable nanofabrication. High-resolution transmission electron microscopy (HRTEM) (Figure 3a3–c3) reveals highly crystalline Ge lattices with a 0.33-nm interplanar spacing corresponding to the (111) plane of cubic Ge (JCPDS No. 04-0545) [45]. Energy-dispersive X-ray spectroscopy (EDS) elemental mapping results (Figure 3a4–c4) show that homogeneous Ge is uniformly distributed and Cu is completely removed, further proving the phase-pure transformation. By implementing dimension-controlled templating, our interfacial redox engineering approach achieves near-perfect structural replication, which can be universally extended to architecting nanostructures of various alloy materials (e.g., Sb, Bi, Sn) (Figures S6 and S7).

2.2 | Dimension-Dependent Electrochemical Performance

The breakthrough synthesis of multidimensional germanium enables pioneering investigations into dimensional effects, unveiling the intrinsic relationship between material performance and structural dimensions. Germanium-based materials have emerged as ideal candidates for anode materials in

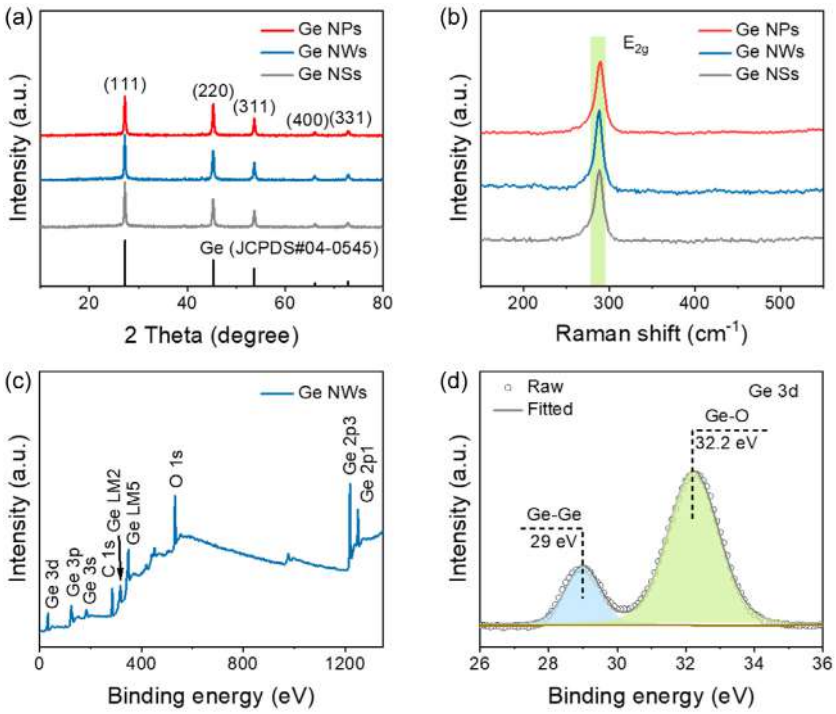


FIGURE 2 | Structural characterization of Ge NPs, Ge NWs, and Ge NSs. (a) XRD patterns and (b) Raman spectra of Ge NPs, Ge NWs, and Ge NSs. (c) XPS survey spectrum and (d) high-resolution Ge 3d spectrum of Ge NWs.

26884062, 2026, 1, Downloaded from https://onlinelibrary.wiley.com/doi/10.1002/sstr.202500755, Wiley Online Library on [06/11/2026]. See the Terms and Conditions (https://onlinelibrary.wiley.com/terms-and-conditions) on Wiley Online Library for rules of use; OA articles are governed by the applicable Creative Commons License

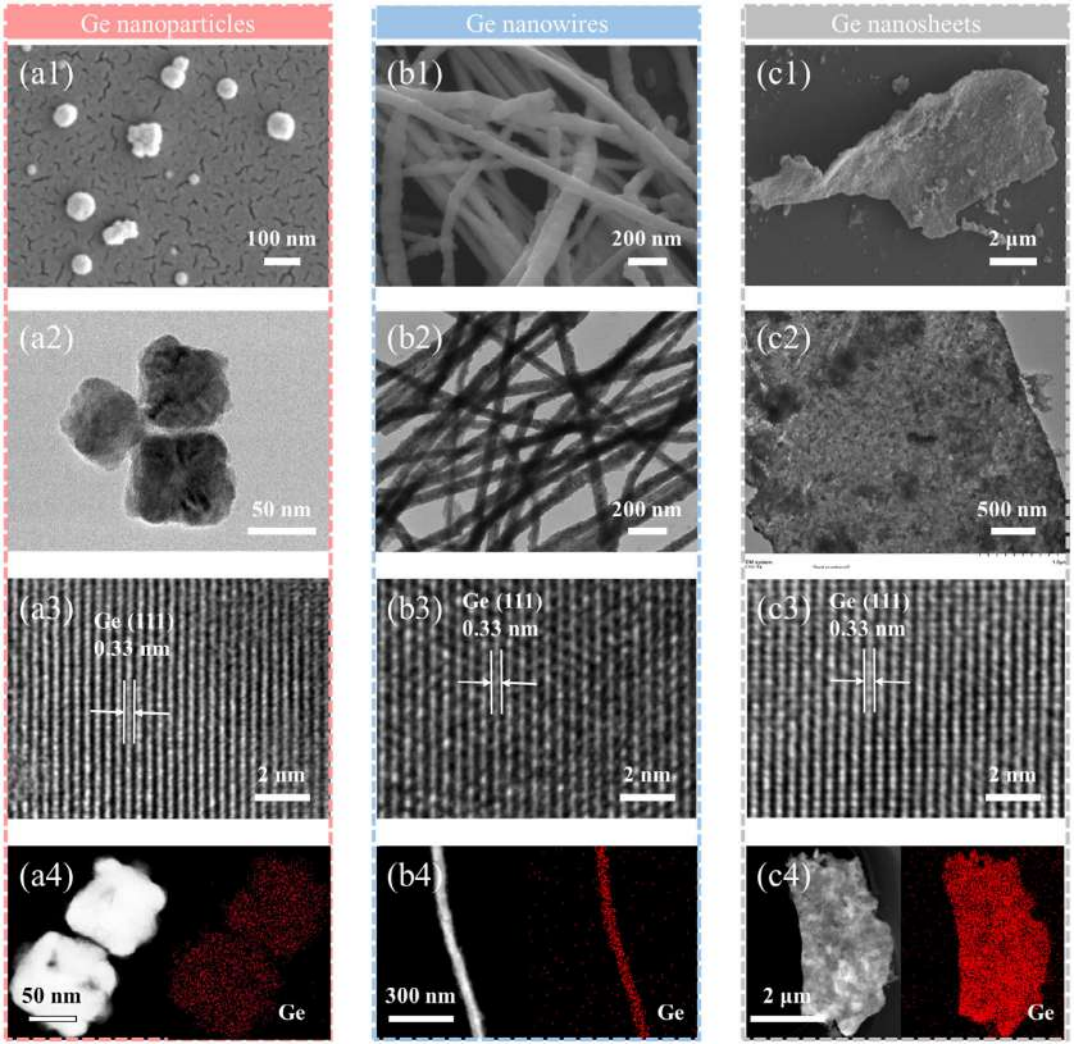


FIGURE 3 | Morphological characterization of Ge NPs, Ge NWs, and Ge NSs. SEM, TEM, HRTEM images, and elemental mapping of Ge NPs (a1–a4), Ge NWs (b1–b4), and Ge NSs (c1–c4).

lithium-ion batteries (LIBs) due to their high theoretical capacity (1384 mAh g^{-1}) and exceptional electrical conductivity (10^4 times higher than that of silicon) [3, 40, 46, 47]. Therefore, this study selects nanostructured germanium as the core model to investigate the correlations between multidimensional structure and properties in electrode materials for LIBs. Figure 4 compares the electrochemical performance of dimensionally engineered Ge anodes (NW, NP, NS) with that of bulk Ge anodes (1–10 μm, Figures S8 and S9). Electrochemical tests were performed in a 1 M $LiPF_6$ dissolved in EC/DEC (1:1 v/v) electrolyte within a voltage window of 0.01–1.5 V vs. Li/Li^+. The first cathodic peak (0.1 mV s^{-1}, Figure 4a) observed at approximately 0.64 V is associated with the formation of the solid electrolyte interface (SEI) layer and associated side reactions occurring at the electrode/electrolyte interface. Within the voltage range of 0.4 and 0.01 V, these peaks can be attributed to the alloying reaction between Ge and Li, resulting in the formation of Li*x*Ge alloys ($xLi + Ge \rightarrow Li_xGe$ ($0 \leq x \leq 4.4$)) [24]. During the anodic scan, three dealloying peaks at 0.43, 0.56, and 0.87 V correspond to the sequential phase transitions: $Li_{22}Ge_5 \rightarrow Li_7Ge_2 \rightarrow Li_9Ge_4 \rightarrow Ge$, indicating the multistep transformation kinetics [12]. Subsequent cycles exhibit stable CV curves without obvious peak shifts, confirming the excellent reversibility of the Ge NW electrodes during lithium insertion/extraction processes [48–50].

The cycling stability of the three Ge nanostructures and bulk Ge for lithium storage at a current density of 0.2 A g^{-1} is illustrated in Figure 4b. The variation in initial capacity is closely aligned with the specific surface area, which governs the number of active sites and the electrode–electrolyte contact area. The BET surface area follows the order: Ge NWs > Ge NPs > Ge NSs > Bulk Ge (Table S2), a trend that is fully consistent with the observed initial capacity. Furthermore, all three types of Ge nanostructured anodes exhibit superior cycling stability to bulk Ge anodes after 100 cycles, demonstrating the inherent superiority of nanostructural design in mitigating electrode degradation. More significantly, among these nanostructures, Ge NW anodes deliver the highest capacity retention (82.6%, 1157.6 mAh g^{-1}), surpassing both Ge NP (78.9%, 967.4 mAh g^{-1}) and Ge NS (80.6%, 807.3 mAh g^{-1}) anodes. The exceptional cycling stability of Ge NWs stems from their 3D percolation network, which actively regulates volumetric strain during cycling, thereby inhibiting pulverization and boosting ionic/electron transport kinetics [51, 52]. As shown in Figure 4c, Ge NWs

26884062, 2026, 1, Downloaded from https://onlinelibrary.wiley.com/doi/10.1002/sstr.202500755, Wiley Online Library on [06/11/2026]. See the Terms and Conditions (https://onlinelibrary.wiley.com/terms-and-conditions) on Wiley Online Library for rules of use; OA articles are governed by the applicable Creative Commons License

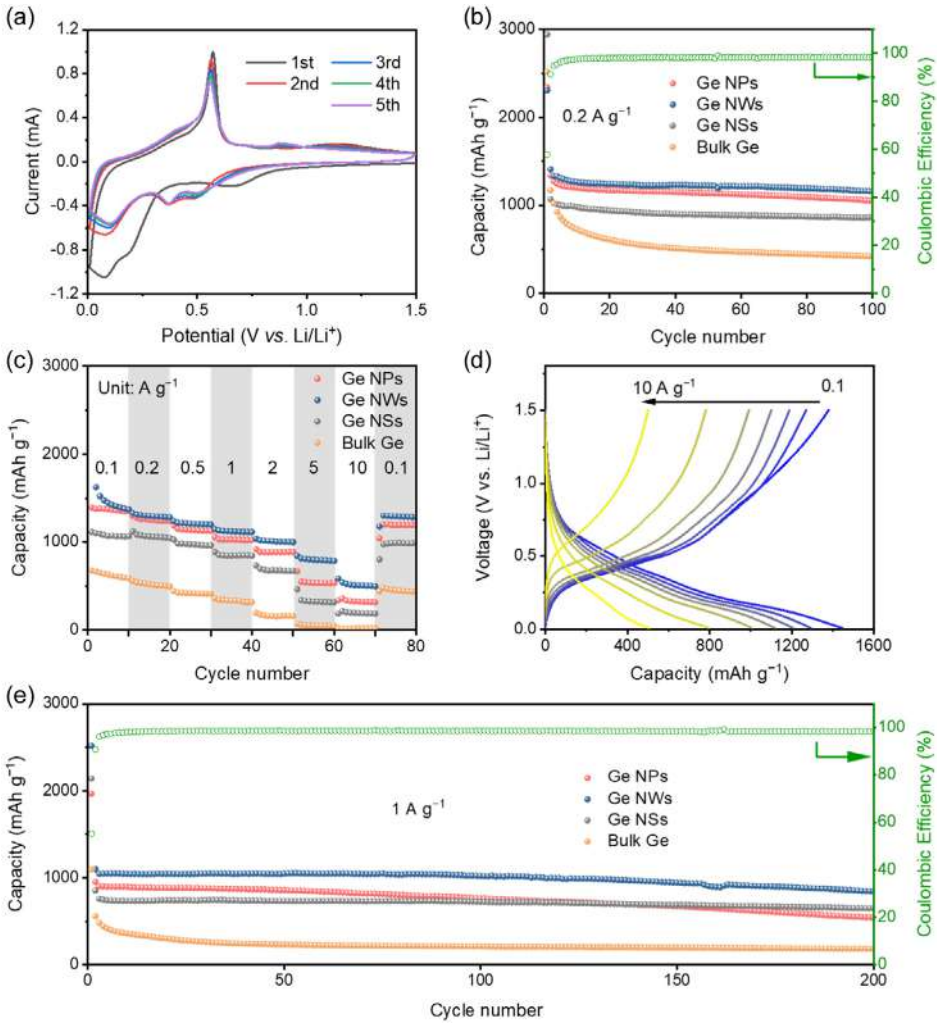


FIGURE 4 | Electrochemical performance of Ge NPs, Ge NWs, Ge NSs, and bulk Ge as anodes in LIBs. (a) CV curves of Ge NW anodes between 0.01 and 1.5 V at a scan rate of 0.1 mV s^{-1}. (b) Comparison of the cycling performance at 0.2 A g^{-1} and (c) rate performance under various current densities from 0.1 to 10 A g^{-1} of Ge NP, Ge NW, Ge NS, and bulk Ge anodes. (d) Galvanostatic charge/discharge curves of Ge NW anodes corresponding to the current densities measured in (c). (e) Long-term cycling performance of Ge NP, Ge NW, Ge NS, and bulk Ge anodes at a current density of 1 A g^{-1}.

anodes achieve specific capacities of 1446.7, 1295.4, 1206.9, 1118.5, 1007.1, and 797.2 mAh g^{-1} at progressively increasing current densities of 0.1, 0.2, 0.5, 1, 2, and 5 A g^{-1}, respectively. Notably, even at an ultrahigh rate of 10 A g^{-1}, Ge NW anodes retained a capacity of 516.9 mAh g^{-1}, which is 24.2 times higher than that of bulk Ge (21.4 mAh g^{-1}) and substantially surpasses the capacities of Ge NP (326.1 mAh g^{-1}) and Ge NS (193.5 mAh g^{-1}) anodes. As the current density increases from 0.1 to 10 A g^{-1}, the discharge plateau of Ge NWs anodes shortens, with a concurrent rise in polarization (which remains significantly lower than that of bulk Ge, Figures 4d and S10). Such enhanced rate performance can be attributed to the dimensionally optimized 3D percolation network in NW electrodes, wherein the cross-linked architecture establishes unimpeded ionic/electronic conduction pathways. Specifically, the 3D interconnected porous structure shortens Li^+ diffusion length, while the long and continuous nanowire network enhances electron conduction.

Ge NW electrodes maintain a capacity of 841.3 mAh g^{-1} after 200 cycles at 1 A g^{-1}, which is 4.6 times higher than the 181.1 mAh g^{-1} observed for bulk Ge, highlighting the nanostructural benefits (Figure 4e). Meanwhile, Ge NP and Ge NS electrodes retain capacities of 541.2 mAh g^{-1} (3.0 times higher) and 646.8 mAh g^{-1} (3.6 times higher), respectively. These findings not only emphasize the superior structural stability of Ge nanostructures during extended cycling but also underscore their significant performance enhancement compared to bulk Ge.

To elucidate the mechanisms governing the exceptional performance of Ge NW anodes, comprehensive electrochemical analyses were carried out. The ion transport kinetics were investigated via scan-rate-dependent CV curves (ranging from 0.1 to 1 mV s^{-1}, Figure S11). For Ge NW anodes, kinetic analysis was performed based on the CV curves (Figure S11b) using the power-law relationship [41, 53, 54]:

$$i = av^b$$

The *b*-values of 0.63 for the oxidation peak O and 0.83 for the reduction peak R (Figure S12a) suggest a mixed charge storage mechanism involving both diffusion-controlled processes (characterized by a *b*-value approaching 0.5) and capacitive-controlled processes (indicated by a *b*-value close to 1) [55, 56]. The capacity contribution

26884062, 2026, 1, Downloaded from https://onlinelibrary.wiley.com/doi/10.1002/sstr.202500755, Wiley Online Library on [06/11/2026]. See the Terms and Conditions (https://onlinelibrary.wiley.com/terms-and-conditions) on Wiley Online Library for rules of use; OA articles are governed by the applicable Creative Commons License

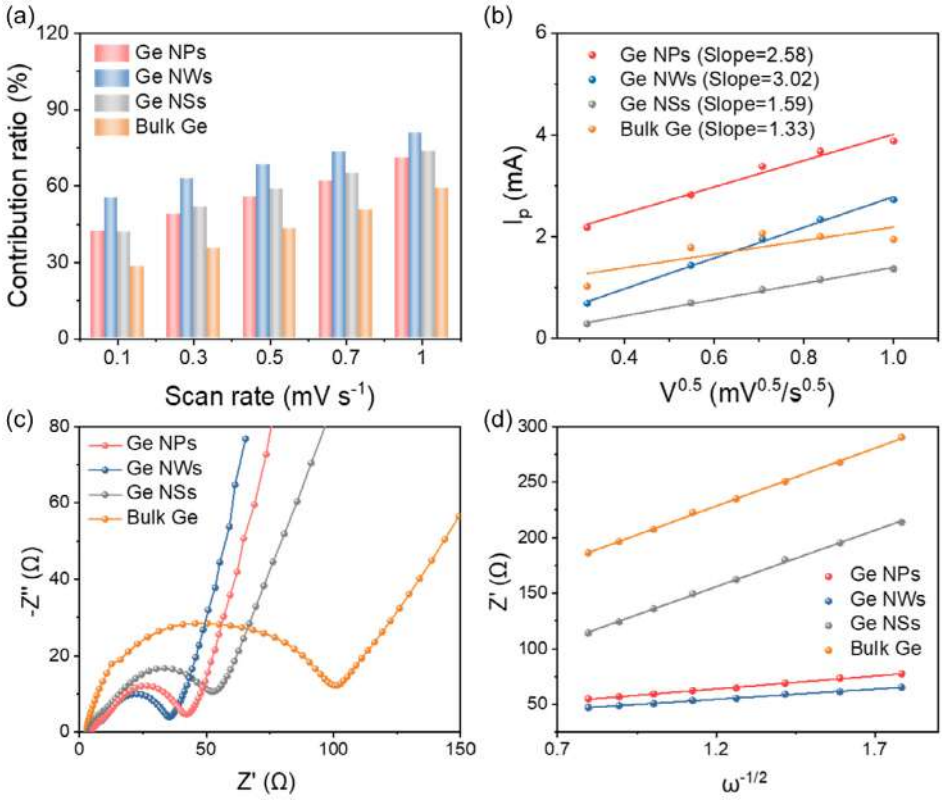


FIGURE 5 | Kinetics analysis of the electrochemical behavior of Ge NP, Ge NW, Ge NS, and bulk Ge anodes. (a) Contribution ratio of the capacitive process at different scan rates, (b) the peak current versus (scan rate)$^{0.5}$ plots and the corresponding linear fits, (c) Nyquist plots (0.05–1,000,000 Hz), and (d) Z'-$\omega^{-1/2}$ plots after 10 cycles at 1 A g^{-1}.

from diffusion- and capacitive-controlled can be quantitatively distinguished using the following equation [57, 58]:

$$i(V) = k_1 v + k_2 v^{1/2}$$

As shown in Figure 5a, the scan rate increases from 0.1 to 1 mV s^{-1}, the capacitive contribution ratios of the Ge NP, Ge NW, Ge NS, and bulk Ge electrodes progressively increase. The capacitive contribution ratios reach 80.7% for Ge NW, 71.1% for Ge NP, and 73.6% for Ge NS anodes, compared to 59.0% for bulk Ge anodes at 1 mV s^{-1}, thereby highlighting the nanostructure-driven surface reactivity (Figures 5a and S12b). These findings confirm that dimensional engineering shifts the charge storage mechanism from a diffusion-controlled process to one dominated by capacitive-controlled processes.

The ion diffusion coefficients were quantitatively evaluated using CV curves (Figures 5b and S11) by employing the Randles–Sevcik equation [59–61]:

$$i_p = 2.69 \times 10^5 A C_{Li} D_{Li}^{1/2} n^{3/2} v^{1/2}$$

The Li^+ diffusion coefficients (D_{Li^+}) were obtained by performing linear fits on i_p vs $V^{\frac{1}{2}}$ plots. Ge NW anodes demonstrated superior kinetics, as evidenced by a slope of 3.02, which is significantly higher than those of Ge NPs (2.58), Ge NSs (1.59), and bulk Ge anodes (1.33) (Figure 5b). This finding is in excellent agreement with the rate test results. The enhanced electrochemical kinetics can be further elucidated through EIS analysis under open-circuit conditions. As shown in Figure 5c, the Nyquist plots of cycled electrodes display clear frequency-dependent features: a semicircular arc in the high-to-medium frequency range attributed to ohmic resistance (R_s) and charge transfer resistance (R_{ct}), followed by a linear Warburg region in the low-frequency domain that reflects solid-state Li^+ diffusion processes [62, 63]. Equivalent circuit modeling (Figure S13) quantitatively reveals that nanostructure markedly improves interfacial kinetics, with Ge NW anodes showing the greatest enhancement. The fitted parameters (Table S3) reveal a 52.56% reduction in R_{ct} values (from 76.14 Ω for bulk Ge to 36.12 Ω for Ge NW anodes). Additionally, the Warburg coefficient (σ) [64, 65] derived from the Z'-$\omega^{-1/2}$ plots (Figure 5d) decreases by 82.26% (from 104.16 to 18.48 Ω s$^{-0.5}$), providing strong evidence for accelerated charge transfer and ion diffusion kinetics. As presented in Figure S14 and Table S4, the σ of the Ge NW anodes exhibited a slight increase with cycling progress, whereas the R_{ct} continuously decreased. Notably, even after 500 cycles, R_{ct} remained at a low level (less than 24 Ω), indicating that the Ge NW anodes possess rapid interfacial charge transfer kinetics and excellent interfacial stability, which are highly advantageous for achieving superior cycling performance.

The galvanostatic intermittent titration technique (GITT) reveals distinct relaxation behaviors in the transient voltage responses during current pulses [66, 67], as shown in Figure S15a, demonstrating discernible differences in relaxation behavior among various nanostructures. The improvement in diffusivity is further substantiated through the application of diffusion equation [68]:

$$D_{Li^+} = \frac{4}{\pi\tau}\left(\frac{m_B V_M}{M_B}\right)^2 \left(\frac{\Delta E_s}{\Delta E_\tau}\right)^2$$

26884062, 2026, 1, Downloaded from https://onlinelibrary.wiley.com/doi/10.1002/sstr.202500755, Wiley Online Library on [06/11/2026]. See the Terms and Conditions (https://onlinelibrary.wiley.com/terms-and-conditions) on Wiley Online Library for rules of use; OA articles are governed by the applicable Creative Commons License

The D_{Li^+} was calculated to be 1.85×10^{-13} cm^2 s^{-1} for Ge NW anodes, based on the above equation involving the relaxation time τ, molar volume V_M (13.58 cm^3 mol^{-1}), and molar mass M_B (72.64 g mol^{-1}). This value is 1.4 times higher than that of Ge NP (1.28×10^{-13} cm^2 s^{-1}) and 2.1 times higher than that of Ge NS anodes (8.87×10^{-14} cm^2 s^{-1}) (Figure S15b and Table S5). The in situ reaction resistance values (602.47 Ω for Ge NW vs 827.54 Ω for Ge NP and 1290.15 Ω for Ge NS anodes, Figure S15c and Table S5) also validating that one-dimensional (1D) nanowire structures are conducive to enhancing ion/electron transport.

3 | Conclusion

In summary, this study presents a structural inheritance-driven synthesis of multidimensional Ge nanostructures via galvanic replacement reaction using dimensionally targeted Cu templates. The developed approach enables facile and rapid preparation of phase-pure Ge nanomaterials with programmable architectures (0D NPs, 1D NWs, 2D NSs), achieving high yield and exceptional morphological retention. The Ge nanostructures exhibited electrochemical performance significantly surpassing that of bulk Ge. Notably, the nanowire structure demonstrated the most superior lithium storage characteristics: (i) outstanding cyclability (841.3 mAh g^{-1} after 200 cycles at 1 A g^{-1}, 4.6 times higher than bulk Ge); (ii) reduced interfacial resistance (R_{ct} = 36.12 Ω, a 52.56% decrease compared to bulk Ge); and (iii) ultrafast ion diffusion (1.85×10^{-13} cm^2 s^{-1}). The 3D percolation network in nanowires synergistically addresses critical challenges in alloy-type anodes by incorporating stress-adaptive porous architectures for volume expansion accommodation, efficient ion/electron percolation pathways, and maximization of electrochemically active surfaces. This dimension-controlled paradigm is universally applicable to alloy-type nanomaterial systems (Sb/Bi/Sn), establishing a materials-by-design platform that paves the way for next-generation high-power lithium-ion batteries.

4 | Experimental Section

4.1 | Synthesis of Copper Templates

4.1.1 | Copper Nanoparticles (Cu NPs)

Cu NPs were synthesized via thermal decomposition [69] following an adapted protocol. In an argon-filled glovebox, a precursor solution was prepared by dissolving 0.1 g (1 mmol) CuCl and 0.2 g (0.74 mmol) octadecylamine (ODA) in 2 mL squalane at 200°C for 30 min. Separately, 19 mL oleylamine (OLA) and 1 mL trioctylphosphine (TOP) were degassed in a three-neck flask (50 mL) under argon. The solution was rapidly heated to 330°C, followed by swift injection of the Cu precursor. After maintaining at 330°C for 3 min, the reaction was quenched in a water bath. The product was purified via triple centrifugation (8,000 rpm, 5 min) with toluene dispersion.

4.1.2 | Copper Nanowires (Cu NWs)

Cu NWs were hydrothermally synthesized [59] by mixing 0.5 mmol D-(+)-glucose, 0.3 mmol $CuCl_2 \cdot 2H_2O$, and 1.9 mmol hexadecylamine (HDA) in 20 mL DI water under vigorous magnetic stirring for 6 h, and the suspension was transferred to a Teflon-lined autoclave and heated at 140°C for 10 h. The resultant nanowires were washed sequentially with warm DI water (60°C), ethanol, acetone, and hexane, followed by vacuum drying.

4.1.3 | Copper Nanosheets (Cu NSs)

Cu NSs were fabricated through mechanical exfoliation [70]. The sandwich-structured Al foil/Cu foil/Al foil (20 μm Al/6 μm Cu) assembly was subjected to repeated rolling-folding-rolling cycles via roll-pressing technology until the Cu layer thickness was reduced to less than 100 nm. The composite foil was etched in 1 M NaOH (150 mL, 5 h) to remove the Al, followed by ultrasonication (30 min) and centrifugation to collect the Cu NSs.

4.2 | Synthesis of Germanium Nanostructures

Ge nanomaterials were synthesized via a galvanic replacement reaction. For Ge NWs, 0.5 mmol Cu NWs and 0.6 mmol GeI_2 were dispersed in 15 mL DMPU within an Ar-filled glovebox. The mixture was heated at 240°C for 8 h under an argon atmosphere, then cooled naturally. Ge NPs/NSs were synthesized using the identical synthetic process with the Cu templates replaced by Cu NPs/NNs. Products were centrifuged (8,000 rpm, 5 min), washed with ethanol, and vacuum-dried.

4.3 | Material Characterization

Crystalline structure was analyzed by XRD (PANalytical X'Pert Pro, Cu Kα λ = 1.54178 Å) and Raman spectroscopy (Horiba XploRA ONE, 532 nm laser). Morphology was examined using SEM (JEOL JSM-7500F, 5 kV) and TEM (JEOL JEM-2100, 200 kV) with EDS mapping. Surface chemistry was investigated by XPS (Thermo ESCALAB 250Xi, Al Kα).

4.4 | Electrochemical Characterization

Electrode slurries were prepared by mixing active material, Ketjenblack ECP600JD, and carboxymethyl cellulose (CMC) (7:2:1 wt%) in DI water. The slurry was coated on Cu foil (mass loading: 1 mg cm^{-2}) and dried at 60°C for 12 h. CR2032 cells were assembled with Li foil as the counter electrodes and 1 M $LiPF_6$ in EC/DEC (1:1 v/v) as electrolyte. Testing methods included the following: (1) galvanostatic cycling: 0.05–1.5 V vs. Li/Li^+ (Neware MIHW-200-160CH); (2) GITT: 0.5 A g^{-1} pulses (20 min) with 2 h relaxation intervals; (3) CV: scan rates of 0.1–1 mV s^{-1}; (4) EIS: frequency range from 100 kHz to 0.01 Hz (Autolab 302N).

Author Contributions

B.P., Y.Q., Y.L., and B.Z. conceptualized the research framework and designed experimental protocols. B.P., Y.Q., and Y.L. developed the initial manuscript draft. The synthetic methodology optimization for multidimensional Ge nanomaterials was jointly conducted by B.P., Y.Q., and Y.L. Material characterization, including XRD, SEM/TEM, Raman spectroscopy, XPS, and electrochemical evaluations, was performed by B.P., Y.Q., Y.W., L.Z., R.S., and B.Z. Schematic illustrations of synthesis routes were created by B.P., Y.Q., and B.Z. through collaborative design. Data interpretation and theoretical analysis were carried out by B.P., Y.Q., Y.L., and B.Z. The research program was supervised by Y.L., B.Z., and W.Y.,

26884062, 2026, 1, Downloaded from https://onlinelibrary.wiley.com/doi/10.1002/sstr.202500755, Wiley Online Library on [06/11/2026]. See the Terms and Conditions (https://onlinelibrary.wiley.com/terms-and-conditions) on Wiley Online Library for rules of use; OA articles are governed by the applicable Creative Commons License

who also critically revised the manuscript. All authors participated in result discussions, provided substantive feedback on successive drafts, and approved the final version for publication.

Acknowledgments

This work was supported by the National Natural Science Foundation of China (52272228), the Science and Technology Department project of Sichuan Province of China (2024ZYD0013), Sichuan Provincial Natural Science Foundation (2025ZNSFSC0145), and the Fundamental Research Funds for the Central Universities (2682025CX003 and 2682024CX050). The authors thank the Analytical & Testing Center of Southwest Jiaotong University for SEM and TEM characterization support.

Conflicts of Interest

W.Y., Y.Q., Q.T., J.B., and Y.L. have filed a Chinese patent application (CN202210640203.1) covering the multidimensional germanium nanomaterials and their application in lithium-ion batteries described in this manuscript. The other authors declare no competing financial interests.

Data Availability Statement

The data that support the findings of this study are available from the corresponding author upon reasonable request.

References

1. D. Carolan, "Recent Advances in Germanium Nanocrystals: Synthesis, Optical Properties and Applications," *Progress in Materials Science* 90 (2017): 128–158.

2. D. D. Vaughn and R. E. Schaak, "Synthesis, Properties and Applications of Colloidal Germanium and Germanium-Based Nanomaterials," *Chemical Society Reviews* 42 (2013): 2861–2879.

3. X. Liu, X.-Y. Wu, B. Chang, and K.-X. Wang, "Recent Progress on Germanium-Based Anodes for Lithium Ion Batteries: Efficient Lithiation Strategies and Mechanisms," *Energy Storage Materials* 30 (2020): 146–169.

4. S. Feng, X. Li, C. Shang, L. Tang, and J. Zhang, "Germanium Based Glass Modified by Graphene as Anode Material with High Capacity for Lithium-Ion Batteries," *Journal of Non-Crystalline Solids* 646 (2024): 123257.

5. J.-N. Lin, Y.-J. Chen, W.-T. Kuo, et al., "Synthesis and Characterization of at-Home Dental Bleaching GeI Incorporating Ge/GeO_{2-x} Nanoparticles," *Ceramics International* 51 (2025): 34321–34328.

6. X. Liu, K. Zhang, Q. Wang, et al., "Three-Dimensional Honeycomb-Like Porous Carbon Embedded with Ge Nanoparticles Anode Composites for Ultrastable Lithium Storage," *Journal of Alloys and Compounds* 939 (2023): 168759.

7. H. Mu, Y. Liu, S. R. Bongu, et al., "Germanium Nanosheets with Dirac Characteristics as a Saturable Absorber for Ultrafast Pulse Generation," *Advanced Materials* 33 (2021): 2101042.

8. M. M. Lazarević, N. L. Ignjatović, Q. Mahlet, et al., "Biocompatible Germanium-Doped Hydroxyapatite Nanoparticles for Promoting Osteogenic Differentiation and Antimicrobial Activity," *ACS Applied Nano Materials* 7 (2024): 8580–8592.

9. I. B. Belyaev, I. V. Zelepukin, P. A. Kotelnikova, et al., "Laser-Synthesized Germanium Nanoparticles as Biodegradable Material for Near-Infrared Photoacoustic Imaging and Cancer Phototherapy," *Advanced Science* 11 (2024): 2307060.

10. Y. Zhang, R. Huang, H. Li, et al., "Triple-Mode Emissions with Invisible Near-Infrared After-Glow from Cr^{3+}-Doped Zinc Aluminum Germanium Nanoparticles for Advanced Anti-Counterfeiting Applications," *Small* 16 (2020): 2003121.

11. L. Seravalli, C. Ferrari, and M. Bosi, "Germanium Nanowires as Sensing Devices: Modelization of Electrical Properties," *Nanomaterials* 11 (2021): 507.

12. H. Liu, T. Wu, L. Zhang, et al., "Germanium Nanowires via Molten-Salt Electrolysis for Lithium Battery Anode," *ACS Nano* 16 (2022): 14402–14411.

13. J.-H. Choi, J.-Y. Moon, and J.-H. Lee, "Controlled Growth of Highly Stable and Conducting Ge Core/ BCN Shell Nanowire," *Ceramics International* 50 (2024): 15994–15999.

14. S. Gao, T. Zhao, D. Wang, J. Huang, Y. Xiang, and Y. Yu, "Ge Nanowires on Top of a Ge Substrate for Applications in Anodes of Li and Na Ion Batteries: A First-Principles Study," *RSC Advances* 12 (2022): 9163–9169.

15. A. Garcia-Gil, S. Biswas, and J. D. Holmes, "A Review of Self-Seeded Germanium Nanowires: Synthesis, Growth Mechanisms and Potential Applications," *Nanomaterials* 11 (2021): 2002.

16. E. Scalise, A. Sarikov, L. Barbisan, et al., "Thermodynamic Driving Force in the Formation of Hexagonal-Diamond Si and Ge Nanowires," *Applied Surface Science* 545 (2021): 148948.

17. J. Yuan, X. Wang, Y. Liu, et al., "Excellent Nonlinear Absorption Properties of 2D Germanium Nanosheets in the Infrared Band," *Optical Materials* 125 (2022): 112115.

18. N. Hussain, Y. Yisen, R. Ur Rehman Sagar, et al., "Quantum-Confined Blue Photoemission in Strain-Engineered Few-Atomic-Layer 2D Germanium," *Nano Energy* 83 (2021): 105790.

19. M. Ge, M. Zong, D. Xu, et al., "Freestanding Germanene Nanosheets for Rapid Degradation and Photothermal Conversion," *Materials Today Nano* 15 (2021): 100119.

20. Y. Xu, Q. Lu, D. Ke, et al., "Topological Transformation of Hydrogen-Terminated Germanium to Germanium Nanosheets for Fast Lithium Storage," *ACS Applied Materials & Interfaces* 16 (2024): 33396–33403.

21. Y. Yang, S. Liu, X. Bian, J. Feng, Y. An, and C. Yuan, "Morphology- and Porosity-Tunable Synthesis of 3D Nanoporous SiGe Alloy as a High-Performance Lithium-Ion Battery Anode," *ACS Nano* 12 (2018): 2900–2908.

22. S. Choi, J. Kim, N.-S. Choi, M. G. Kim, and S. Park, "Cost-Effective Scalable Synthesis of Mesoporous Germanium Particles via a Redox-Transmetalation Reaction for High-Performance Energy Storage Devices," *ACS Nano* 9 (2015): 2203–2212.

23. D. Kwon, J. Ryu, M. Shin, et al., "Synthesis of Dual Porous Structured Germanium Anodes with Exceptional Lithium-Ion Storage Performance," *Journal of Power Sources* 374 (2018): 217–224.

24. S. Yan, H. Song, S. Lin, H. Wu, Y. Shi, and J. Yao, "GeO_2 Encapsulated Ge Nanostructure with Enhanced Lithium-Storage Properties," *Advanced Functional Materials* 29 (2019): 1807946.

25. Y. Chen, Y. Zou, X. Shen, et al., "Ge Nanoparticles Uniformly Immobilized on 3D Interconnected Porous Graphene Frameworks as Anodes for High-Performance Lithium-Ion Batteries," *Journal of Energy Chemistry* 69 (2022): 161–173.

26. H. Yu, M. Gao, M. Zhou, et al., "F127/PDA Dual-Assisted Fabricating High Dispersed Ge Nanoparticles/N-Doped Porous Carbon Composites with Efficient Lithium Storage," *Journal of Materials Research and Technology* 26 (2023): 5055–5064.

27. E. Rusman, A. Nulu, and K. Y. Sohn, "N-Doped Cnt Assisted GeO_2–Ge Nanoparticles as a High-Capacity and Durable Anode Material for Lithium-Ion Batteries," *RSC Advances* 15 (2025): 28841–28852.

28. M. Gu, H. Yang, D. E. Perea, J.-G. Zhang, S. Zhang, and C.-M Wang, "Bending-Induced Symmetry Breaking of Lithiation in Germanium Nanowires," *Nano Letters* 14 (2014): 4622–4627.

29. I. Erofeev, K. Saidov, Z. Baraissov, et al., "3D Shape Reconstruction of Ge Nanowires during Vapor–Liquid–Solid Growth under Modulating Electric Field," *ACS Nano* 18 (2024): 22855–22863.

26884062, 2026, 1, Downloaded from https://onlinelibrary.wiley.com/doi/10.1002/sstr.202500755, Wiley Online Library on [06/11/2026]. See the Terms and Conditions (https://onlinelibrary.wiley.com/terms-and-conditions) on Wiley Online Library for rules of use; OA articles are governed by the applicable Creative Commons License

30. Y.-L. Sun, X.-D. Zheng, W. Jevasuwan, and N. Fukata, "ZnO/Ge Core–Shell Nanowires and Ge Nanotubes Fabricated by Chemical Vapor Deposition and Wet Etching," *Nanotechnology* 33 (2022): 325602.

31. S. Li, C. Chen, K. Fu, et al., "Nanosized Ge@CNF, Ge@C@CNF and Ge@CNF@C Composites via Chemical Vapour Deposition Method for Use in Advanced Lithium-Ion Batteries," *Journal of Power Sources* 253 (2014): 366–372.

32. J. Hao, Y. Yang, J. Zhao, et al., "Ionic Liquid Electrodeposition of Strain-Released Germanium Nanowires as Stable Anodes for Lithium Ion Batteries," *Nanoscale* 9 (2017): 8481–8488.

33. Z. Yu, D. Wang, M. Lu, J. Li, X. Meng, and H. Li, "$Ti_3C_2T_x$ Mxene Coated 3D Ordered Macroporous Germanium Anodes for Li-Ion Batteries with Enhanced Cycling Stability and Fast Li-Ion Mobility," *Materials Research Bulletin* 182 (2025): 113138.

34. S. Kilian, K. McCarthy, K. Stokes, et al., "Direct Growth of Si, Ge, and Si-Ge Heterostructure Nanowires Using Electroplated Zn: An Inexpensive Seeding Technique for Li-Ion Alloying Anodes," *Small* 17 (2021): 2005443.

35. K. Stokes, H. Geaney, G. Flynn, M. Sheehan, T. Kennedy, and K. M. Ryan, "Direct Synthesis of Alloyed $Si_{1-x}Ge_x$ Nanowires for Performance-Tunable Lithium Ion Battery Anodes," *ACS Nano* 11 (2017): 10088–10096.

36. X.-M. Pham, S. Abdul Ahad, N. N. Patil, H. Geaney, S. Singh, and K. M. Ryan, "Binder-Free Germanium Nanoparticle Decorated Multi-Wall Carbon Nanotube Anodes Prepared Via Two-Step Electrophoretic Deposition for High Capacity Li-Ion Batteries," *Nanoscale Horizons* 9 (2024): 637–645.

37. R. C. Miller, J. R. Neilson, and A. L. Prieto, "Amide-Assisted Synthesis of Iron Germanium Sulfide (Fe_2GeS_4) Nanostars: The Effect of $LiN(SiMe_3)_2$ on Precursor Reactivity for Favoring Nanoparticle Nucleation or Growth," *Journal of the American Chemical Society* 142 (2020): 7023–7035.

38. Y. H. Kim, J. H. An, X. Li, et al., "Solvent-Driven Transformation of Microsized Metal Particles into a Nanoporous Structure and Its Application to Ultrafast-Charging Batteries," *Advanced Functional Materials* 33 (2023): 2301552.

39. M. Liu, X. Ma, L. Gan, Z. Xu, D. Zhu, and L. Chen, "A Facile Synthesis of a Novel Mesoporous Ge@C Sphere Anode with Stable and High Capacity for Lithium Ion Batteries," *Journal of Materials Chemistry A* 2 (2014): 17107–17114.

40. A. C. Serino, J. S. Ko, M. T. Yeung, et al., "Lithium-Ion Insertion Properties of Solution-Exfoliated Germanane," *ACS Nano* 11 (2017): 7995–8001.

41. C. C. Li, B. Wang, D. Chen, et al., "Topotactic Transformation Synthesis of 2D Ultrathin GeS_2 Nanosheets toward High-Rate and High-Energy-Density Sodium-Ion Half/Full Batteries," *ACS Nano* 14 (2020): 531–540.

42. N. Liu, K. Xu, Y. Lei, et al., "Germanene Nanosheets: Achieving Superior Sodium-Ion Storage via Pseudointercalation Reactions," *Small Structures* 2 (2021): 2100041.

43. R. Liu, F. Luo, L. Zeng, et al., "Dual Carbon Decorated Germanium-Carbon Composite as a Stable Anode for Sodium/Potassium-Ion Batteries," *Journal of Colloid and Interface Science* 584 (2021): 372–381.

44. D. T. Ngo, R. S. Kalubarme, H. T. T. Le, et al., "Carbon-Interconnected Ge Nanocrystals as an Anode with Ultra-Long-Term Cyclability for Lithium Ion Batteries," *Advanced Functional Materials* 24 (2014): 5291–5298.

45. D. Tang, H. Yu, J. Zhao, et al., "Bottom-up Synthesis of Mesoporous Germanium as Anodes for Lithium-Ion Batteries," *Journal of Colloid and Interface Science* 561 (2020): 494–500.

46. F. Wu, J. Maier, and Y. Yu, "Guidelines and Trends for Next-Generation Rechargeable Lithium and Lithium-Ion Batteries" *Chemical Society Reviews* 49 (2020): 1569–1614.

47. L. C. Loaiza, L. Monconduit, and V. Seznec, "Si and Ge-Based Anode Materials for Li-, Na-, and K-Ion Batteries: A Perspective from Structure to Electrochemical Mechanism," *Small* 16 (2020): 1905260.

48. I. M. Gavrilin, Y. O. Kudryashova, A. A. Kuz'mina, et al., "High-Rate and Low-Temperature Performance of Germanium Nanowires Anode for Lithium-Ion Batteries," *Journal of Electroanalytical Chemistry* 888 (2021): 115209.

49. A. Garcia, S. Biswas, D. McNulty, et al., "One-Step Grown Carbonaceous Germanium Nanowires and Their Application as Highly Efficient Lithium-Ion Battery Anodes," *ACS Applied Energy Materials* 5 (2022): 1922–1932.

50. M. S. Seifner, M. Sistani, F. Porrati, et al., "Direct Synthesis of Hyperdoped Germanium Nanowires," *ACS Nano* 12 (2018): 1236–1241.

51. J. Hao, Y. Wang, Q. Guo, J. Zhao, and Y. Li, "Structural Strategies for Germanium-Based Anode Materials to Enhance Lithium Storage," *Particle & Particle Systems Characterization* 36 (2019): 1900248.

52. D. Li, H. Wang, T. Zhou, W. Zhang, H. K. Liu, and Z. Guo, "Unique Structural Design and Strategies for Germanium-Based Anode Materials Toward Enhanced Lithium Storage," *Advanced Energy Materials* 7 (2017): 1700488.

53. A.-G. Nguyen, H. T. T. Le, R. Verma, D.-L. Vu, and C.-J. Park, "Boosting Sodium-Ion Battery Performance Using an Antimony Nanoparticle Self-Embedded in a 3D Nitrogen-Doped Carbon Framework Anode," *Chemical Engineering Journal* 429 (2022): 132359.

54. S. Zheng, H. Huang, Y. Dong, et al., "Lonogel-Based Sodium Ion Micro-Batteries with a 3D Na-Ion Diffusion Mechanism Enable Ultrahigh Rate Capability," *Energy & Environmental Science* 13 (2020): 821–829.

55. L. Liu, L. Gui, R. Hu, et al., "Bi-Doped Commercial Hard Carbon with Enhanced Slope Capacity to Deliver Superior Rate Performance for Sodium-Ion Batteries," *ACS Applied Energy Materials* 8 (2025): 4211–4219.

56. S. Li, X. Lu, Y. Li, et al., "Dynamic Lock-and-Release Mechanism Enables Reduced ΔG at Low Temperatures for High-Performance Polyanionic Cathode in Sodium-Ion Batteries," *Advanced Materials* 36 (2024): 2413013.

57. T. Brezesinski, J. Wang, S. H. Tolbert, and B. Dunn, "Ordered Mesoporous Alpha-MoO_3 with Iso-Oriented Nanocrystalline Walls for Thin-Film Pseudocapacitors," *Nature Materials* 9 (2010): 146–151.

58. X. Shen, Q. Zhou, M. Han, et al., "Rapid Mechanochemical Synthesis of Polyanionic Cathode with Improved Electrochemical Performance for Na-Ion Batteries," *Nature Communications* 12 (2021): 2848.

59. B. Pu, Y. Liu, J. Bai, et al., "Iodine-Ion-Assisted Galvanic Replacement Synthesis of Bismuth Nanotubes for Ultrafast and Ultrastable Sodium Storage," *ACS Nano* 16 (2022): 18746–18756.

60. Z. Yu, X. Jia, H. Gao, et al., "Unlocking Interfacial Dynamics of Porous Electrode via Vertical-Aligned Bismuth-Nanosheet Decorating for Vanadium Redox Flow Batteries," *Advanced Functional Materials* 35 (2024): 2420534.

61. X. Wu, Z. Li, W. Feng, et al., "Insights into Electrolyte-Induced Temporal and Spatial Evolution of an Ultrafast-Charging Bi-Based Anode for Sodium-Ion Batteries," *Energy Storage Materials* 66 (2024): 103219.

62. R. Mo, Z. Lei, D. Rooney, and K. Sun, "Three-Dimensional Double-Walled Ultrathin Graphite Tube Conductive Scaffold with Encapsulated Germanium Nanoparticles as a High-Areal-Capacity and Cycle-Stable Anode for Lithium-Ion Batteries," *ACS Nano* 13 (2019): 7536–7544.

63. Y. Huang, X. Hu, J. Li, et al., "Rational Construction of Heterostructured Core-Shell Bi_2S_3@Co_9S_8 Complex Hollow Particles toward High-Performance Li- and Na-Ion Storage," *Energy Storage Materials* 29 (2020): 121–130.

64. Y.-R. Zhu, Y. Xie, R.-S. Zhu, et al., "Kinetic Study on $LiFePO_4$-Positive Electrode Material of Lithium-Ion Battery," *Ionics* 17 (2011): 437–441.

26884062, 2026, 1, Downloaded from https://onlinelibrary.wiley.com/doi/10.1002/sstr.202500755, Wiley Online Library on [06/11/2026]. See the Terms and Conditions (https://onlinelibrary.wiley.com/terms-and-conditions) on Wiley Online Library for rules of use; OA articles are governed by the applicable Creative Commons License

65. D. Qu, G. Wang, J. Kafle, et al., "Electrochemical Impedance and Its Applications in Energy-Storage Systems," *Small Methods* 2 (2018): 1700342.

66. Z.-Y. Gu, J.-M. Cao, J.-Z. Guo, et al., "Hybrid Binder Chemistry with Hydrogen-Bond Helix for High-Voltage Cathode of Sodium-Ion Batteries," *Journal of the American Chemical Society* 146 (2024): 4652–4664.

67. Z. Y. Gu, J. Z. Guo, J. M. Cao, et al., "An Advanced High-Entropy Fluorophosphate Cathode for Sodium-Ion Batteries with Increased Working Voltage and Energy Density," *Advanced Materials* 34 (2022): 2110108.

68. J. Zhou, H. Zhao, N. Lin, et al., "Silicothermic Reduction Reaction for Fabricating Interconnected Si-Ge Nanocrystals with Fast and Stable Li-Storage," *Journal of Materials Chemistry A* 8 (2020): 6597–6606.

69. H.-J. Yang, S.-Y. He, H.-L. Chen, and H.-Y. Tuan, "Monodisperse Copper Nanocubes: Synthesis, Self-Assembly, and Large-Area Dense-Packed Films," *Chemistry of Materials* 26 (2014): 1785–1793.

70. H. Liu, H. Tang, M. Fang, et al., "2D Metals by Repeated Size Reduction," *Advanced Materials* 28 (2016): 8170–8176.

Supporting Information

Additional supporting information can be found online in the Supporting Information section. **Supporting Fig. S1:** XRD patterns of Cu NPs, Cu NWs and Cu NSs. **Supporting Fig. S2:** SEM and TEM images of Cu NPs (**a1**, **a2**), Cu NWs (**b1**, **b2**) and Cu NSs (**c1**, **c2**). **Supporting Fig. S3:** XRD patterns of Ge NWs using (**1**) TOP and (**2**) DMPU as the solvent for the galvanic replacement reaction. **Supporting Fig. S4:** XRD patterns of Ge NWs using DMPU as the solvent for the galvanic replacement reaction. **Supporting Fig. S5:** (**a**) SEM image and (**b**) magnified view of Ge NSs. **Supporting Fig. S6:** (**a**) XRD patterns, (**b**) SEM and (**c**) TEM images of Sb NPs. **Supporting Fig. S7:** (**a**) XRD patterns, (**b**) SEM and (**c**) TEM images of Bi NPs. **Supporting Fig. S8:** XRD pattern of bulk Ge. **Supporting Fig. S9:** (**a**) SEM and (**b**) TEM images of bulk Ge. **Supporting Fig. S10:** Voltage profiles corresponding to the rate performance test (**Figure 4** (**c**)) of bulk Ge. **Supporting Fig. S11:** Cyclic voltammetry (CV) curves of (**a**) Ge NPs, (**b**) Ge NWs, (**c**) Ge NSs, and (**d**) bulk Ge at different scan rates. **Supporting Fig. S12:** (**a**) b values according to log (scan rate) and log (peak current) of the oxidation peak and reduction peak and (**b**) contribution ratio at 1 mV s^{-1} of the Ge NW electrodes. **Supporting Fig. S13:** The equivalent circuit model used to fit the obtained EIS date. **Supporting Fig. S14:** The Nyquist plots of the Ge NW electrodes after different number of cycles. **Supporting Fig. S15:** (**a**) Quasi-equilibrium voltage curves from GITT tests, (**b**) Li^+ diffusion coefficients (D_{Li}^+) and (**c**) reaction residence of Ge NPs, Ge NWs and Ge NSs. **Supporting Table S1:** Reduction potentials of Cu and Ge relative to the standard hydrogen electrode (SHE). **Supporting Table S2:** BET specific surface area of the synthesized Ge nanostructures and bulk Ge. **Supporting Table S3:** EIS fitting values of the Ge NP, Ge NW, Ge NS, and Bulk Ge electrodes after the same cycle. **Supporting Table S4:** EIS fitting values of the Ge NW electrodes after different number of cycles. **Supporting Table S5:** Li^+ diffusion coeffcient and reaction resistance average values of the Ge NP, Ge NW, and Ge NS electrodes were obtained from **Figure S13.**

26884062, 2026, 1, Downloaded from https://onlinelibrary.wiley.com/doi/10.1002/sstr.202500755, Wiley Online Library on [06/11/2026]. See the Terms and Conditions (https://onlinelibrary.wiley.com/terms-and-conditions) on Wiley Online Library for rules of use; OA articles are governed by the applicable Creative Commons License